Range-Point Migration-Based Image Expansion Method Exploiting Fully Polarimetric Data for UWB Short-Range Radar

doi: 10.1109/TGRS.2017.2776274

Range Points Migration Based Image Expansion Method Exploiting Fully Polarimetric Data for UWB Short Range Radar

Ayumi Yamaryo, *Non-member,* Tatsuo Takatori, *Non-member,* Shouhei Kidera, *Member, IEEE,* and Tetsuo Kirimoto, *Senior Member, IEEE,*

***Abstract*—Ultra wideband (UWB) radar with high range resolution is a promising technology for use in short-range 3-dimensional (3-D) imaging applications, in which optical cameras are not applicable. One of the most efficient 3-D imaging methods is the range point migration (RPM) method, which has a definitive advantage for synthetic aperture radar (SAR) approach in terms of computational burden, high accuracy and high spatial resolution. However, if an insufficient aperture size or angle is provided, these kind of method cannot reconstruct the whole target structure, due to absence of reflection signals from large part of target surface. To expand the 3-D image obtained by RPM, this paper proposes an image expansion method by incorporating the RPM feature and fully polarimetric data based machine learning approach. Following ellipsoid-based scattering analysis and learning with a neural network, this method expresses the target image as an aggregation of parts of ellipsoids, which significantly expands the original image by the RPM method without sacrificing reconstruction accuracy. The results of numerical simulation based on 3-D finite difference time domain (FDTD) analysis verify the effectiveness of our proposed method, in terms of image expansion criteria.**

***Index Terms*—UWB radars, Short range sensing, 3-D sensors, Fully polarimetric analysis, Range Points Migration(RPM), Image expansion**

I. Introduction

ULtra wideband(UWB) pulse radar is expected to be adopted in innovative short-range sensing techniques, such as robotic sensors in disaster rescue situations or private watch sensors for independently living elderly or disabled persons. To provide accurate high resolution 3-D images, researchers have investigated various radar imaging methods based on data synthesis, such as synthetic aperture radar(SAR) [1], time-reversal algorithms [2], [3], and range migration methods [4], [5], [6]. However, all of these methods incur impractically large computational costs, particularly in 3-D imaging problems, and their reconstruction accuracies are insufficient to capture the detailed structures of target shapes. As a different approach, the method [7] has been developed, which is based on reversible transforms, namely, boundary scattering transform (BST). While this method achieves a fast 3-D imaging in specifying boundary extraction, it suffers from serious accuracy degradation in noisy or interfered cases assuming multiple or complex-shaped targets due to being based on the difference operation of observed ranges. In contrast, the range point migration(RPM) method extracts the 3-D target boundary even in noisy or richly interfered case [8], [9], [10]. The RPM method assesses the distribution function of the direction of arrival (DOA) for each observed range point (denoted as a set of antenna location and range), and does not require any paring procedure of discrete range points as pre-processing. It also accomplishes highly accurate 3-D imaging for general target shape in far less computation costs than that required by conventional signal synthesis approaches such as 3-D beamforming or SAR based reconstruction scheme. The effectiveness of RPM has been widely reported in short-range radar and acoustic imaging studies [11], [12], [13]. However, the image reproduction area obtained by RPM and other conventional methods is, usually severely limited by an available aperture angle, determined by the aperture size and distance to target, which is itself restricted by obstacles such as rubble in disaster zones and indoor sensing problems. For these reasons, the reconstructed area frequently becomes too narrow to identify the target structure, and this is an essential problem in any kind of imaging methods as far as they use only direct reflection signal for imaging.

To alleviate this problem, an image expansion method based on ellipse expansion has been proposed [14]. In the method [14], a target such as human body is approximated by an aggregate of ellipsoids representing the head, trunk and limbs, each clustered RPM image is then expanded to a single ellipsoid. the method [14] uniquely computes the ellipsoid fitting in data space (constituted by the range points) rather than in real space, avoiding the errors introduced by the RPM imaging process. Although the method [14] accurately expands ellipsoidal targets even in noisy situations, shapes that significantly differ from ellipsoids (such as tori and cylinder) are naturally degraded by the expansion.

To address the above problem, this paper proposes a novel image expansion algorithm by incorpolating the RPM feature and fully polarimetric data based machine learning. Namely, our goal is more efficient and reliable expansion from the original RPM image with fully polarimetric data. While some studies for incorporating polarimetric data and RPM method, for super-resolution range data extraction [15] or accuracy improvement [16], have been investigated, there are no study for the challenge of image expansion using fully polarimetric data. There are several studies for polarimetric analysis for short range sensing issue [17], [19], [20]. Such literature reveal that the fully polarimetric data exploitation has a possibility to offer significant improvement for image reconstruction. For

A. Yamaryo is with Communication Systems Center Mitsubishi Electric Corp., Japan. T. Takatori, S. Kidera and T. Kirimoto are with the Graduate School of Informatics and Engineering, The University of Electro-Communications, Tokyo, Japan. E-mail: kidera@uec.ac.jp

more particular investigation for improving RPM image, this paper tries to relate the fully polarimetric data in the time domain to the target structure focusing on single ellipsoid. According to this analysis, the fully polarimetric data can reveal the axial radii and rotation angles of the ellipsoids. Furthermore, several significant ellipsoidal parameters can be acquired by a neural network at a single antenna location.

Finally, we expanded the image from the target points obtained by the RPM method, fitting an aggregation of partial ellipsoidal surface estimated by the fully polarimetric data to each RPM point. Note that, the multiple partial ellipsoids based image expansion, proposed in this paper, is done by exploiting the RPM feature such as one-to-one correspondence between range point and target point This approach fundamentally differs from the conventional one, which relies on fitting a single ellipsoid [14], and is effective for not-ellipsoidal shape without sacrificing accuracy degradation. Utilized on data generated in finite-difference time-domain (FDTD) simulations, the proposed method yielded a significantly more expanded target image than did the original RPM method, even for non-elliptical objects.

II. System Model

Figure 1 shows the system model. An omni-directional antenna is scanned on the x-y plane, where each location is defined as $(X, Y, 0)$. The mono-static radar is assumed. The transmitted signal as current source is defined as mono-cycle pulse with center wavelength λ. It assumes the multiple linear polarizations for the x and y directions in transmitting and receiving, respectively. $s'_{i,j}(X, Y, t)$ denotes the received electric field at the location $(X, Y, 0)$, at time t, when the transmitting and receiving polarization are along the i(x or y) axis and j(x or y) axis, respectively. $\tilde{s}_{i,j}(X, Y, t)$ is the output of the Wiener filter of $s'_{i,j}(X, Y, t)$ calculated as;

$$\tilde{s}_{i,j}(X, Y, t) = \int_{-\infty}^{\infty} W(\omega) S'_{i,j}(X, Y, \omega) \mathrm{e}^{\mathrm{j}\omega t} \mathrm{d}\omega, \qquad (1)$$

where $S'_{i,j}(X, Y, \omega)$ is the signal in the frequency domain of $s'_{i,j}(X, Y, t)$. $W(\omega)$ is defined as

$$W(\omega) = \frac{S_{\mathrm{ref}}(\omega)^*}{(1-\eta)S_0^2 + \eta |S_{\mathrm{ref}}(\omega)|^2} S_0, \qquad (2)$$

where $\eta = 1/(1+(S/N)^{-1})$, and $S_{\mathrm{ref}}(\omega)$ is the reference signal in the frequency domain, which is the complex conjugate of that of the transmitted signal. S_0 is a constant for dimension consistency. This filter is an optimal MSE (Mean Square Error) linear filter for additive noises. $\tilde{s}_{i,j}(X, Y, t)$ is now converted to $s_{i,j}(X, Y, R)$ using $R = ct/2\lambda$, where c is the speed of the radio wave. The range point extracted from the local maxima of $s_{x,x}(X, Y, R)$ as to R is denoted as $\boldsymbol{q} = (X, Y, R)$; the details are given in [8].

III. RPM Method and Conventional Expansion Approach

A. Original RPM method

We have already established accurate and high-speed 3-D target boundary extraction method as RPM method, which

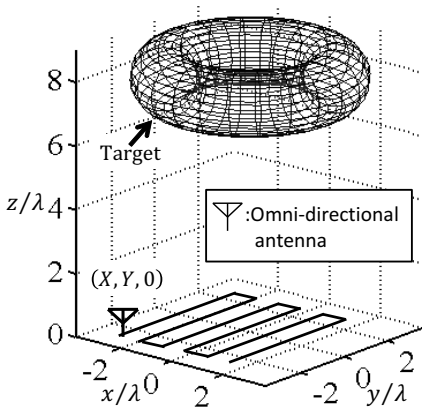

Fig. 1. System model.

can be applicable to various 3-D target shapes having such as concave surface, edges ridges with 1/100 wavelength accuracy [8], [9]. the RPM method method is based on the assumption that a target boundary point (x, y, z) exists on a sphere with its center as the antenna location $(X, Y, 0)$ and its radius as the observed range R. The direction of arrival DOA for each range point $\boldsymbol{q}_i = (X_i, Y_i, R_i)$, can be determined by assessing the spatial accumulation of intersection points of the spheres, whose center is $(X_i, Y_i, 0)$ and radius is R_i. The RPM method determines the target point for range point $\boldsymbol{q}_i$ as:

$$\hat{\boldsymbol{p}}(\boldsymbol{q}_i) = \underset{\boldsymbol{p}^{\mathrm{int}}(\boldsymbol{q}_i;\boldsymbol{q}_l,\boldsymbol{q}_m)\in\mathcal{P}_i}{\arg\max} \sum_{(\boldsymbol{q}_j,\boldsymbol{q}_k)\in\mathcal{Q}_i} g(\boldsymbol{q}_i;\boldsymbol{q}_j,\boldsymbol{q}_k) \times \exp\left\{ -\frac{\|\boldsymbol{p}^{\mathrm{int}}(\boldsymbol{q}_i;\boldsymbol{q}_j,\boldsymbol{q}_k) - \boldsymbol{p}^{\mathrm{int}}(\boldsymbol{q}_i;\boldsymbol{q}_l,\boldsymbol{q}_m)\|^2}{2\sigma_r^2} \right\}, \qquad (3)$$

where $\boldsymbol{p}^{\mathrm{int}}(\boldsymbol{q}_i;\boldsymbol{q}_j,\boldsymbol{q}_k)$ denotes the intersection point among the three spheres, determined by the range points $\boldsymbol{q}_i$, $\boldsymbol{q}_j$ and $\boldsymbol{q}_k$. σ_r is an empirically determined constant. Figure 2 presents the spatial relationship between the three spheres with $\boldsymbol{q}_i$, $\boldsymbol{q}_j$, $\boldsymbol{q}_k$ and its intersection point. The weighting function $g(\boldsymbol{q}_i;\boldsymbol{q}_j,\boldsymbol{q}_k)$ is defined by:

$$g(\boldsymbol{q}_i;\boldsymbol{q}_j,\boldsymbol{q}_k) = s(\boldsymbol{q}_j)\exp\left\{ -\frac{D\left(\boldsymbol{q}_i,\boldsymbol{q}_j\right)^2}{2\sigma_D^2} \right\} + s(\boldsymbol{q}_k)\exp\left\{ -\frac{D\left(\boldsymbol{q}_i,\boldsymbol{q}_k\right)^2}{2\sigma_D^2} \right\}, \qquad (4)$$

where $s(\boldsymbol{q}_j)$ denotes the amplitude of $s(\boldsymbol{q}_j)$ at $R = R_j$ and $D(\boldsymbol{q}_i,\boldsymbol{q}_j) = \sqrt{(X_i - X_j)^2 + (Y_i - Y_j)^2}$ hold. Eq. (4) yields the convergence effect of intersection points with respect to the antenna locations. A set of intersection points as $\mathcal{P}_i$ is defined as ;

$$\mathcal{P}_i = \left\{ \boldsymbol{p}^{\mathrm{int}}(\boldsymbol{q}_i;\boldsymbol{q}_j,\boldsymbol{q}_k) | (\boldsymbol{q}_j,\boldsymbol{q}_k) \in \mathcal{Q}_i \right\}. \qquad (5)$$

$\mathcal{Q}_i$ denotes the investigating region of antenna locations. Note that, each target point regarded denote as $\hat{\boldsymbol{p}}(\boldsymbol{q}_i)$ is associated with each range point $\boldsymbol{q}_i$, which means the one-to-one correspondence between them. While the RPM method accomplishes an accurate and fast 3-D imaging, even in richly

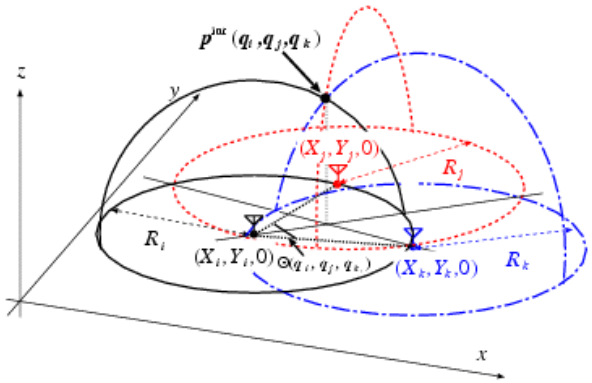

Fig. 2. Relationship among three spheres determined by $\boldsymbol{q}_i$, $\boldsymbol{q}_j$, $\boldsymbol{q}_k$ and its intersection point.

interfered situation caused by multiple target reflection or noisy environment, it (also SAR or others) suffers from an insufficient imaging region, when the aperture size is small. This insufficiency is an essential problem in radar imaging methods, and should be resolved by other approaches, such as an expansion schemes.

B. Single ellipsoid based expansion method

Here we briefly introduce the imaging method conventionally used to expand target image regions [14], which is based on an ellipse expansion of an image obtained by RPM. the method [14] performs ellipse fitting in the data space comprising the antenna location and observed range, which is enabled by the unique feature of RPM imaging [8]. Ellipse fitting of the RPM image in real space is overly sensitive to errors introduced by the RPM imaging process. In contrast, ellipse fitting in data space is essentially impervious to imaging error because the fitting process is directly carried out without through the imaging process, whereas RPM is only employed in image clustering. More specified, the method [14] first uses the target points produced by RPM only for the clustering of the range points, the distribution of which in data space is often very complicated in the case of multiple targets. The clustered range points are then employed for ellipse fitting, which is converted in data space. However, the method [14] assumes that the target is shaped similarly to an ellipse and is inaccurate for significantly dissimilar shapes. The applicability for non-ellipsoidal target, such as target with edge or having multiple reflection points has been also demonstrated[8], where the fatal inaccuracy for expansion has been confirmed. This is natural because of a simple assumption that target should be expressed as a "single " ellipsoid. In addition, multiple targets or complicated target shapes must be correctly clustered; otherwise serious expansion error occurs.

IV. Proposed Method

This section proposes a novel method that exploits the fully polarimetric data, expanding RPM images to variously shaped targets and thereby solving the above-mentioned problem. In many studies, significant information on a target structure or

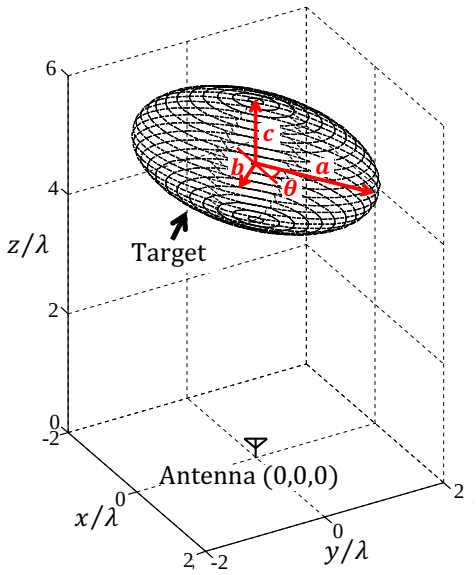

Fig. 3. Observation model for fully polarimetric analysis to a single ellipsoid target.

condition has been obtained by analyzing or decomposing multiple polarimetric SAR images [17], [19], [20]. Thus, the potential of utilizing fully polarimetric data in object or scene detection is well recognized. This paper focuses on the image expansion issue for the reconstructed RPM image, by extracting the polarimetric feature through the time-series data based neural network learning and appropriate fitting algorithm for non-ellipsoidal shape target.

A. Polarimetric analysis for single ellipsoid target

We first investigate the relationship between the time-series waveform of the fully polarimetric data and ellipsoid parameters (axial radius and rotation angle). Figure 3 shows the observation model that is subjected to polarimetric analysis. The target is assumed to be a single ellipsoid centered at $(0, 0, z_c)$. The antenna is located at $(0, 0, 0)$. Here, a, b and c are the radii of the ellipsoid along the x-axis, y-axis and z-axis, respectively, and θ is the rotation angle about the z-axis. The observation data are generated by the FDTD method. Figure 4 shows the Wiener filter output of the received signals $s_{x,x}$, $s_{x,y}$ and $s_{y,y}$ in the time domain, where the parameter a is varied while other parameters are fixed ($b = 1.0\lambda$, $c = 0.5\lambda$ and $\theta = 0°$). In this figure, the amplitudes of $s_{x,x}$ and $s_{y,y}$ are positively correlated with the axial radius a of the ellipsoid, while that of $s_{x,y}$ does not significantly change with axial radius. This fact demonstrates that the amplitude of polarized data along the major axis of an ellipsoid is directly related to an expansion for ellipsoid, where the x-y polarized data does not affect significantly, and this indicates that $s_{x,x}$ and $s_{y,y}$ contributes the size estimation of target shape. Figure 5 shows the Wiener filter output of the received signal $s_{x,y}$ when θ is varied and the other parameters are fixed as $a = 3.0\lambda$,

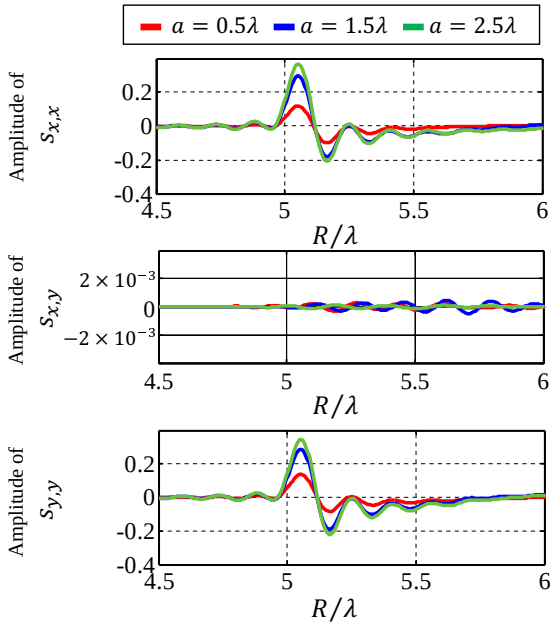

Fig. 4. Outputs of the Wiener filter $s_{x,x}(0,0,R)$, $s_{x,y}(0,0,R)$, and $s_{y,y}(0,0,R)$ when a is variable and other parameters are fixed as $b = 1\lambda$, $c = 0.5\lambda$ and $\theta = 0°$.

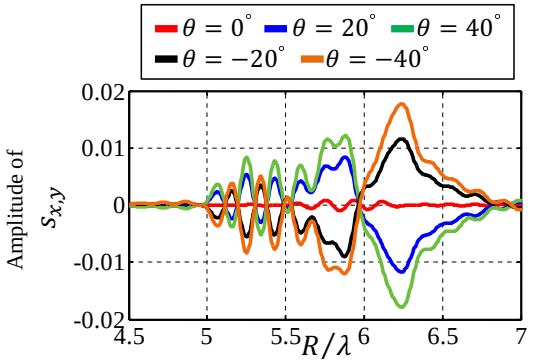

Fig. 5. Outputs of the Wiener filter $s_{x,y}(0,0,R)$ when θ is variable and other parameters are fixed as $a = 3\lambda$, $b = 2\lambda$ and $c = 0.5\lambda$.

$b = 2.0\lambda$ and $c = 0.5\lambda$. Figure 5 also shows that an amplitude of $s_{x,y}$ data significantly increases according to target rotation to maximum at $45°$. The received amplitude of $s_{x,y}$ strongly correlates with the rotation angle; moreover, the sign of the phase indicates the rotation direction. Therefore, the rotation angle of the ellipsoid can be estimated from the $s_{x,y}$ signal. The fully polarimetric data, especially those of the time-series waveform, contain important information on both the local structure and global expanse of the target shape. Then, one RPM imaging point with no size can be expanded by partial ellipsoidal surface if such information can be extracted by fully polarimetric data.

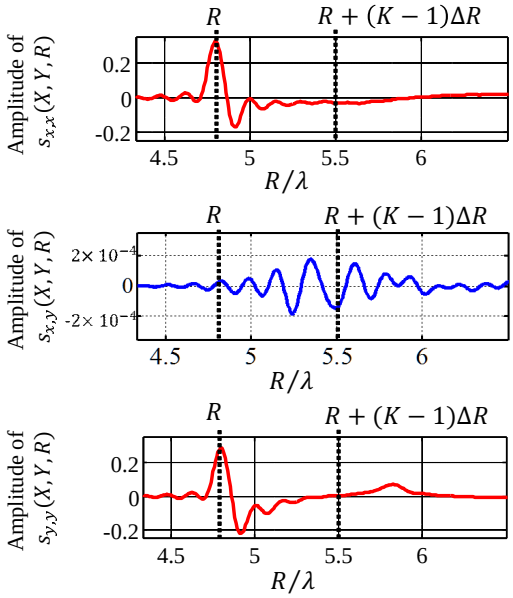

Fig. 6. Extraction scheme for time-series data in the proposed method.

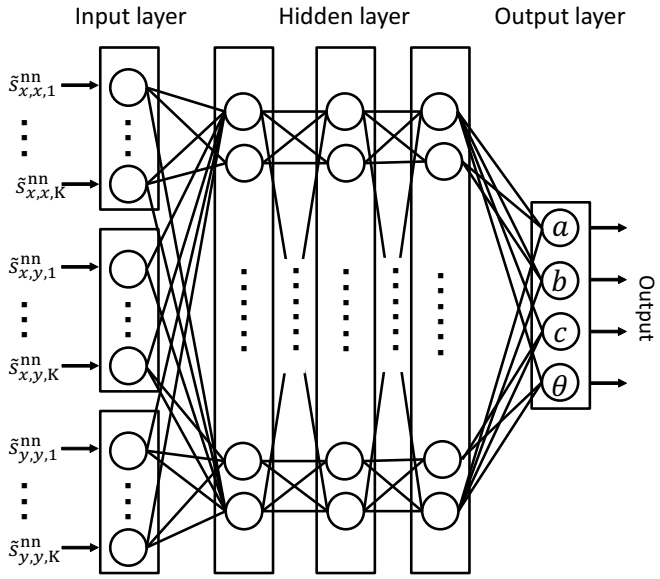

Fig. 7. Layer structure of neural network in the proposed method.

B. Neural network learning for fully polarimetric data

Based on previous analysis, the proposed method first prepares a time-series dataset of various ellipsoids with their a, b, c and θ parameters. These parameters make important role in the expansion process, because the proposed method relies on the expansion with an aggregation of ellipsoid. Thus, a full polarimetric data for each range point needs to be associated with ellipsoid, the part of which expresses the local boundary of actual object. In this method, such association has been achieved via neural network based training process as follows.

Note that, when one considers a reflection data from ellipsoid object, there is a creeping wave propagating along backside of object. However, the strength of this component is much smaller than that of direct reflection, e.g. specular reflection, then, we deal with the time-series data with a finite length. To generate the input data for the windowed time-series data, we defined an input vector $\boldsymbol{s}^{\rm nn}_{i,j}(X,Y,R)(i=x,y,j=x,y)$ for each range point $\boldsymbol{q}=(X,Y,R)$:

$$\begin{aligned}\boldsymbol{s}^{\rm nn}_{i,j}(X,Y,R) \quad \equiv \quad & [s_{i,j}(X,Y,R), s_{i,j}(X,Y,R+\Delta R), \\ & \cdots, s_{i,j}(X,Y,R+(K-1)\Delta R)] \end{aligned} \tag{6}$$

where ΔR corresponds to the time window scale, and K is a constant natural number. Figure 7 shows the structure of the neural network. In the training sequence, the input data of the received signal of the antenna located at $(0,0,0)$, namely, $(X,Y)=(0,0)$ are used, for simplicity, where the ellipsoid parameters (a,b,c,θ) are varied.

These parameters significantly depend on the amplitude of the input signal. Therefore, when inputting the received data into the trained neural network, the propagation attenuation of the received amplitude must be considered, because the amplitude directly affects the size of ellipsoid in the proposed method. The proposed method compensates for the propagation attenuation of each received signal by applying a function of the measured range R. Theoretically, the amplitude of a signal radiated from a point source is attenuated on the first order of the propagation range. However, in this case, we must consider the reflection signals from various shape of target, and it is generally difficult to estimate an attenuation ratio without knowledge of target shape, theoretically. To address this problem, we investigated the attenuation ratios from various ellipsoids at various distances and calculated the average attenuation ratio. Specifically, the distance from an ellipsoid target to the antenna was rescaled as 1.0λ to 10λ in 1.0λ interval. The antenna was located at $(0,0,0)$, and the observation data are also generated by FDTD. The ellipsoid was postured as shown in Fig. 3. The ellipsoid parameters a, b and c are each varied as $0.5\lambda, 1\lambda, 1.5\lambda, 2\lambda, 2.5\lambda$ and 3λ, while $\theta=0^\circ$ is fixed.

The input time-series data $\tilde{\boldsymbol{s}}^{\rm nn}_{i,j}(X,Y,R)(i=x,y,j=x,y)$ are then compensated as

$$\tilde{\boldsymbol{s}}^{\rm nn}_{i,j}(X,Y,R) = f(R/R_0)\boldsymbol{s}^{\rm nn}_{i,j}(X,Y,R_0) \tag{7}$$

where $f(R/R_0)$ denotes the averaged attenuation ratio and R_0 is the reference distance. Note that, $f(R/R_0)$ is a polynomial function of R/R_0, which is fitted to the logarithm of the above-described dataset.

C. Multiple ellipsoids based image expansion for RPM point

Our image expansion methodology relies on fitting each RPM target point to a partial ellipsoidal surface with parameters estimated by the above neural network approach. In the literature [14], each group of target points obtained by RPM was expanded as a single ellipsoid, which is problematic for shapes that widely differ from ellipsoids. Thus, the proposed method expresses each RPM target point as part of an ellipsoid surface; that is, a single target shape is expressed as an aggregation of partial ellipsoidal surfaces. Figure 8 shows the difference between the conventional and the proposed schemes for image expansion. In this sense, our method differs from that of [14]. Figure 9 illustrates the basic concept of the multiple ellipsoid-based expansion scheme. In the proposed method, the part of each ellipsoid (estimated by each $\boldsymbol{q}_k$ through the trained neural network) is fitted to each RPM point as $\boldsymbol{p}_k$, using LOS direction $\boldsymbol{e}^{\rm n}_k$. Note that, to avoid an over-fitting, only the portion of ellipsoid is used for image expansion.

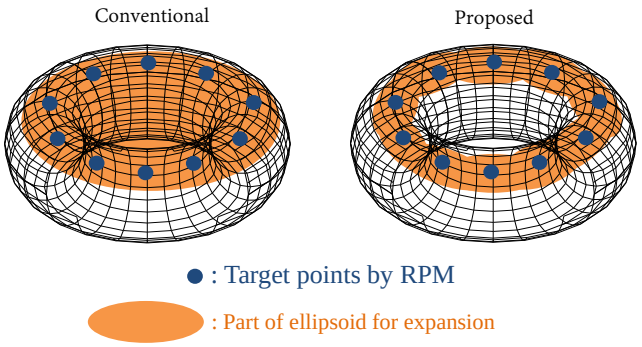

Fig. 8. Scheme comparison between the conventional and the proposed methods.

For appropriate fitting the partial ellipsoid, the ellipsoid boundary points are converted to fit the RPM point and its LOS direction as;

$$\begin{aligned}\begin{pmatrix} x^E_k \\ y^E_k \\ z^E_k \end{pmatrix} &= \begin{pmatrix} \cos\hat{\theta} & -\sin\hat{\theta} & 0 \\ \sin\hat{\theta} & \cos\hat{\theta} & 0 \\ 0 & 0 & 1 \end{pmatrix} \begin{pmatrix} \hat{a}\cos\phi\cos\psi \\ \hat{b}\cos\phi\sin\psi \\ \hat{c}\sin\psi \end{pmatrix} \\ &+ \begin{pmatrix} 0 \\ 0 \\ R_k-(z_c-\hat{c}/2) \end{pmatrix} \end{aligned} \tag{8}$$

where $(\hat{a},\hat{b},\hat{c},\hat{\theta})$ is estimated parameters for the range points $\boldsymbol{q}_k$, and ϕ and ψ are azimuthal and elevation angles of the ellipsoid, respectively. To determine the ellipsoid for each target point, we need to estimate the 9 degree of freedom. In this case, we investigate 4 independent parameters a, b, c and ϕ, and need to determine other 5 parameters from RPM point and its geometrical characteristic. Here, applying RPM to the range points $\boldsymbol{q}_k=(X_k,Y_k,R_k)$, we also estimated a corresponding target point $\boldsymbol{p}_k=(x_k,y_k,z_k)$. Note that each target point $\boldsymbol{p}_k$ satisfies a one-to-one correspondence with each range point $\boldsymbol{q}_k$; this feature is unique to RPM imaging. Under the assumption that the antenna receives a strong echo from the target boundary, which is perpendicular to the line of sight (LOS) direction on $\boldsymbol{p}_k$, the unit vector of the LOS direction, that is, normal vector on target boundary, is calculated as $\boldsymbol{e}_{{\rm n},k}=(\boldsymbol{p}_k-(X_k,Y_k,0))/||\boldsymbol{p}_k-(X_k,Y_k,0)||$. In addition, since the target boundary should be tangent to the plane orthogonal to this normal vector, the expanding ellipsoid should also be tangent to the target boundary. Even in this geometrical condition, the total parameters of ellipsoid cannot be uniquely determined, then, for simplicity, we assume that

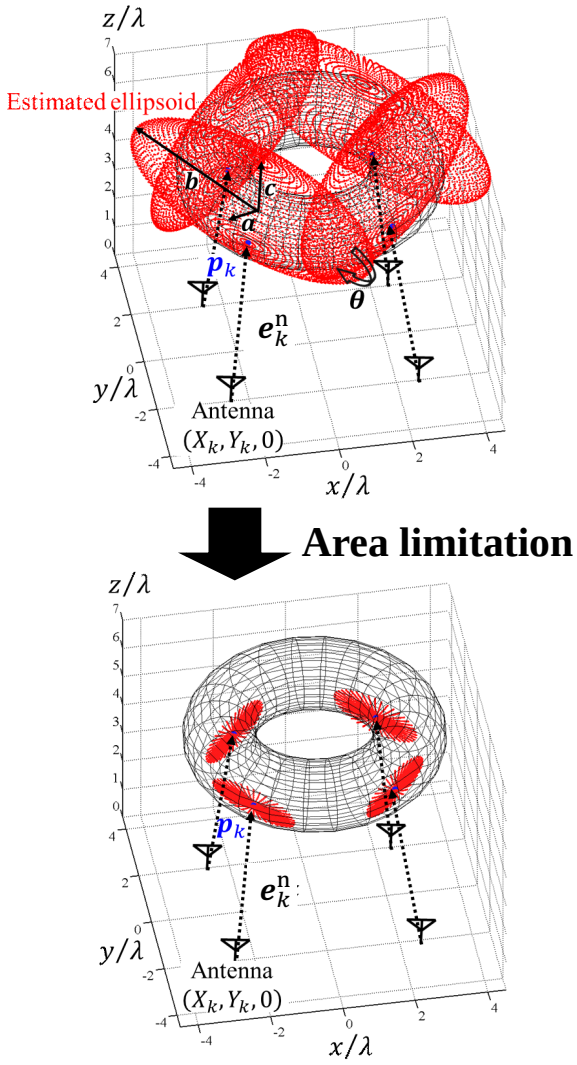

Fig. 9. Example of the expanded result by the proposed method.

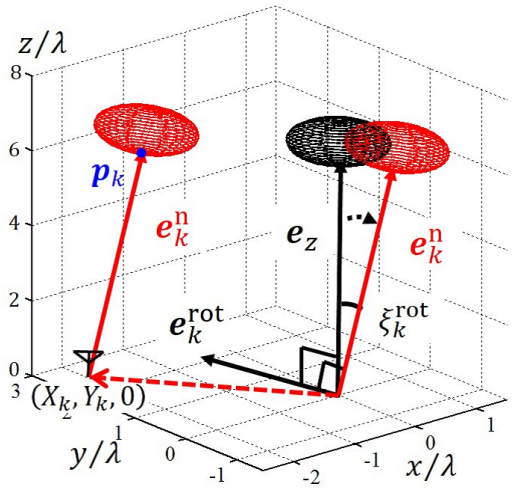

Fig. 10. Ellipsoid rotation and translation along the LOS direction $\boldsymbol{e}_k^{\mathrm{n}}$.

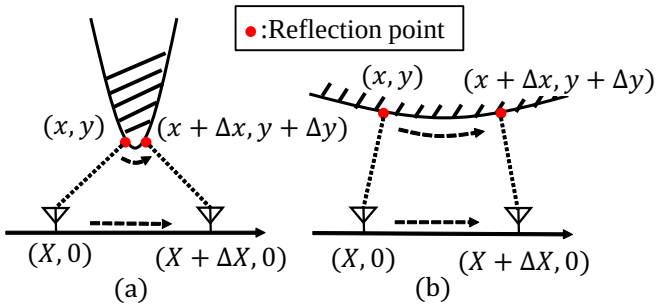

Fig. 11. Relationship between $\Delta x/\Delta X$ and curvature on target surface.

the tangential point of each ellipsoid is located, at an elevation angle $\psi = -\pi/2$.

Then, the LOS direction in the learning process as in Fig. 3, namely, $\boldsymbol{e}_z = (0, 0, 1)$, is converted to that for each range point $\boldsymbol{q}_k$ according to $\boldsymbol{e}_k^{\mathrm{n}}$. According to the conversion, each point (x_k^E, y_k^E, z_k^E) on estimated ellipsoid boundary is also converted as;

$$(\tilde{x}_k^E, \tilde{y}_k^E, \tilde{z}_k^E)^{\mathrm{T}} = \boldsymbol{R}_k(\boldsymbol{e}_k^{\mathrm{rot}}, \xi_k^{\mathrm{rot}})(x_k^E, y_k^E, z_k^E)^{\mathrm{T}} + (X_k, Y_k, 0)^{\mathrm{T}}, \tag{9}$$

where the matrix $\boldsymbol{R}_k(\boldsymbol{e}_k^{\mathrm{rot}}, \xi_k^{\mathrm{rot}})$ denotes 3-dimensional rotation along the axis $\boldsymbol{e}_k^{\mathrm{rot}} = \dfrac{\boldsymbol{e}_z \times \boldsymbol{e}_k^{\mathrm{n}}}{|\boldsymbol{e}_z \times \boldsymbol{e}_k^{\mathrm{n}}|}$ with the angle $\xi_k^{\mathrm{rot}} = \cos^{-1}(\boldsymbol{e}_z \cdot \boldsymbol{e}_k^{\mathrm{n}})$. Specifically, the matrix is calculated as;

$$\boldsymbol{R}_k(\boldsymbol{e}_k^{\mathrm{rot}}, \xi_k^{\mathrm{rot}}) = \begin{pmatrix} C_k(e_{x,k}^{\mathrm{rot}})^2 + \cos\xi_k^{\mathrm{rot}} & C_k e_{x,k}^{\mathrm{rot}} e_{y,k}^{\mathrm{rot}} - e_{z,k}^{\mathrm{rot}} \sin\xi_k^{\mathrm{rot}} & C_k e_{z,k}^{\mathrm{rot}} e_{x,k}^{\mathrm{rot}} + e_{y,k}^{\mathrm{rot}} \sin\xi_k^{\mathrm{rot}} \\ C_k e_{z,k}^{\mathrm{rot}} e_{x,k}^{\mathrm{rot}} - e_{y,k}^{\mathrm{rot}} \sin\xi_k^{\mathrm{rot}} & C_k(e_{y,k}^{\mathrm{rot}})^2 + \cos\xi_k^{\mathrm{rot}} & C_k e_{y,k}^{\mathrm{rot}} e_{z,k}^{\mathrm{rot}} - e_{x,k}^{\mathrm{rot}} \sin\xi_k^{\mathrm{rot}} \\ C_k e_{z,k}^{\mathrm{rot}} e_{x,k}^{\mathrm{rot}} - e_{y,k}^{\mathrm{rot}} \sin\xi_k^{\mathrm{rot}} & C_k e_{y,k}^{\mathrm{rot}} e_{z,k}^{\mathrm{rot}} + e_{x,k}^{\mathrm{rot}} \sin\xi_k^{\mathrm{rot}} & C_k(e_{z,k}^{\mathrm{rot}})^2 + \cos\xi_k^{\mathrm{rot}} \end{pmatrix}, \tag{10}$$

where $\boldsymbol{e}_k^{\mathrm{rot}} = (e_{x,k}^{\mathrm{rot}}, e_{y,k}^{\mathrm{rot}}, e_{z,k}^{\mathrm{rot}})$ and $C_k = 1 - \cos\xi_k^{\mathrm{rot}}$. Figure 10 illustrates the translation and rotation of the ellipse so as to fit the target point $\boldsymbol{p}_k$.

Finally, a part of ellipsoid is extracted as $\hat{\Omega}_k$ for each $\boldsymbol{q}_k$. To accomplish an edge preserving property in expansion process, the proposed method changes a size of portion of ellipsoid, corresponding to curvature radius on target surface. The literature [22] or [23] revealed that the following matrix can assess the curvature radius along each axis;

$$\boldsymbol{S}_k = \begin{bmatrix} \dfrac{\partial x_k}{\partial X_k} & \dfrac{\partial y_k}{\partial X_k} \\ \dfrac{\partial x_k}{\partial Y_k} & \dfrac{\partial y_k}{\partial Y_k} \end{bmatrix} \simeq \begin{bmatrix} \dfrac{\Delta x_k}{\Delta X_k} & \dfrac{\Delta y_k}{\Delta X_k} \\ \dfrac{\Delta x_k}{\Delta Y_k} & \dfrac{\Delta y_k}{\Delta Y_k} \end{bmatrix}, \tag{11}$$

where (x_k, y_k, z_k) denotes the target boundary point estimated by RPM corresponding to $\boldsymbol{q}_k = (X_k, Y_k, R_k)$. Note that, each difference approximation in the right term in Eq. 11 is readily calculated by using the one-to-one relationship between $\boldsymbol{q}_k$ and (x_k, y_k, z_k). Figure 11 shows the relationship between object boundaries with small or large curvature radius, and the value of $\partial y_k/\partial X_k$ in the two-dimensional view. As shown in Fig. 11, $\partial y_k/\partial X_k$ can approximately and simply assess the curvature radius indirectly. Then, the parameter for expansion area is calculated as follows;

$$\phi_k(\psi) = \sqrt{u_k(\psi)^2 + v_k(\psi)^2}\,\phi_{\mathrm{E}} \quad (0 \le \psi \le 2\pi), \quad (12)$$

$$\left(\ u_k(\psi)\ \ v_k(\psi)\ \right)^{\mathrm{T}} = \boldsymbol{U}_k \left(\ \lambda_{1,k}\cos(\psi)\ \ \lambda_{2,k}\sin(\psi)\ \right)^{\mathrm{T}}, \quad (13)$$

where ψ and $\phi_k(\psi)$ denote the elevation and azimuth angles of an expanded ellipsoid, respectively. $\lambda_{1,k}$ and $\lambda_{2,k}$ are eigenvalues of $\boldsymbol{S}_k$, which determine principal curvature on (x_k, y_k, z_k), and $\boldsymbol{U}_k$ is the matrix consisted of eigenvecters of $\boldsymbol{S}_k$. ψ_E is determined empirically. This process enables us to change an expansion area depending on its curvature, namely, an edge preserving is possible.

Then, the expanded image $\hat{\Omega}_{\mathrm{ex}}$ is determined as;

$$\hat{\Omega}_{\mathrm{ex}} = \bigcup_k \hat{\Omega}_k \quad (14)$$

The lower side of Fig. 9 denotes the area limitation example, described above.

After training process through neural network with FDTD data, the actual imaging process in the proposed method is summarized as follows;

Step 1). Target boundary points $\boldsymbol{p}_k = (x_k, y_k, z_k)(k = 1, ..., N_{\mathrm{RP}})$ are obtained by applying the RPM to $\boldsymbol{q}_k = (X_k, Y_k, R_k)$ which is extracted from the local maximum of $s_{x,x}(X_k, Y_k, R_k)$.

Step 2). $\boldsymbol{s}^{\mathrm{nn}}_{i,j,k}(X, Y, R)$ for $\boldsymbol{q}_k$ (uniquely connected with $\boldsymbol{p}_k$) are extracted as in Eq. (6), and are compensated as $\tilde{\boldsymbol{s}}^{\mathrm{nn}}_{i,j,k}(X, Y, R)$ in Eq. (7) corresponding to the observation distance R_k.

Step 3). $\tilde{\boldsymbol{s}}^{\mathrm{nn}}_{i,j,k}(X, Y, R)$ is inputted to the trained neural network for obtaining the parameters of ellipsoid as $(\hat{a}_k, \hat{b}_k, \hat{c}_k, \hat{\theta}_k)$.

Step 4). Each estimated ellipsoid denoted as (x^E_k, y^E_k, z^E_k) is rotated and translated as $(\tilde{x}^E_k, \tilde{y}^E_k, \tilde{z}^E_k)$ so that it fits each target point $\boldsymbol{p}_k = (x_k, y_k, z_k)$ in Eq. (9), and its partial area as $\hat{\Omega}_k$ is extracted.

Step 6). For all range points $\boldsymbol{q}_k$, Step 2) and Step 5) are carried out and generates an each expanded image as $\hat{\Omega}_k$.

Step 7). For the l th discrete member belonging in $\hat{\Omega}_k$, denoted as $\boldsymbol{p}^E_{k,l}$, the following evaluation function is introduced;

$$\zeta(\boldsymbol{p}^E_{k,l}) = \sum_{m,n,(m\neq k)} \exp\left\{-\frac{\|\boldsymbol{p}^E_{k,l} - \boldsymbol{p}^E_{m,n}\|^2}{2\sigma^2_\zeta}\right\} \quad (15)$$

If the following condition is satisfied;

$$\zeta(\boldsymbol{p}^E_{k,l}) \le \gamma \max_{m,n} \zeta(\boldsymbol{p}^E_{m,n}) \quad (16)$$

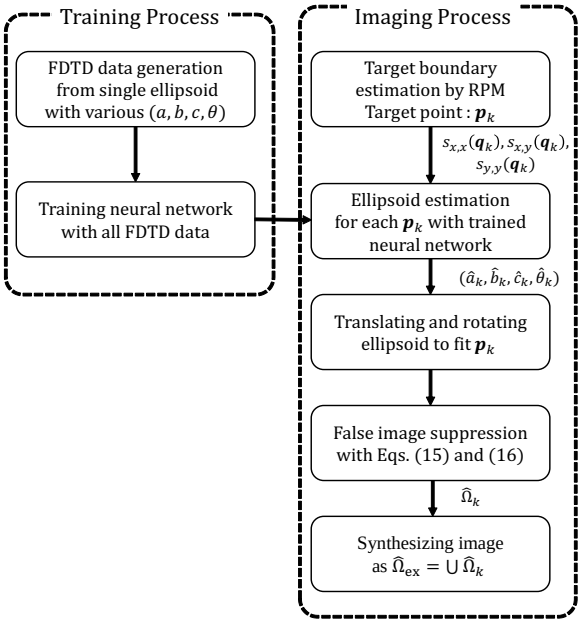

Fig. 12. Flowchart of the proposed method.

The point $\boldsymbol{p}^E_{k,l}$ is remove from $\hat{\Omega}_k$. Final expanded image $\hat{\Omega}_{\mathrm{ex}}$ is expressed as aggregate of $\hat{\Omega}_k$ as in Eq. (14).

Figure 12 outlines the flowchart of the proposed method. Note that, the post-procedure in Step 7) makes role of eliminating the large deviated points in considering the spatial density of all expanded imaging points as $\boldsymbol{p}^E_{k,l}$. The parameter σ_ζ can be determined by considering the assumed sampling interval of each discrete formed ellipsoid. As in this flowchart, once the NN learned the training data generated by the FDTD, the proposed method does not require the FDTD or NN training process for each imaging, which maintains the high-speed 3-D imaging with this method. In addition, the proposed method does not need any clustering scheme for RPM points in advance, which is required in [14]. This is because each ellipsoid is independently assigned to each target point.

V. Performance Evaluation in Numerical Simulation

This section describes the two types of performance evaluations. One is the evaluation for neural network based learning using fully polarimetric data, where unknown parameters of ellipsoid are estimated by the neural network with time-series data base. The other demonstrates the performance of image expansion by our proposed method, namely, multiple ellipsoid based expansion for RPM imaging points.

A. Ellipsoid parameter estimation by neural network

This section reports on the parameter estimation of a single ellipsoid from the fully polarimetric dataset. The antenna is located at $(x, y, z) = (0, 0, 0)$. During the learning stage of the neural network, the parameters a, b and c of the training

TABLE I
ESTIMATION RESULTS FOR THE NEURAL NETWORK BASED PARAMETER ESTIMATION OF SINGLE ELLIPSOID.

True (a/λ,b/λ,c/λ,θ/deg)	Estimated (a/λ,b/λ,c/λ,θ/deg)	Relative error (a,b,c,θ)[%]
(1.70,1.00,2.50,30.0)	(1.72,0.97,2.51,28.0)	(1.14,2.68,0.28,6.76)
(1.50,2.20,3.00,20.0)	(1.51,2.18,3.00,21.7)	(0.85,0.73,0.05,8.53)
(1.00,2.00,2.70,40.0)	(1.01,2.01,2.69,43.2)	(0.62,0.56,0.24,7.99)
(2.00,1.50,1.00,-35.0)	(2.02,1.48,0.97,-37.0)	(0.97,1.48,3.48,5.39)
(1.40,2.80,2.00,10.0)	(1.40,2.82,2.01,9.6)	(0.33,0.64,0.36,3.68)
(2.30,1.50,1.10,20.0)	(2.38,1.47,1.09,19.1)	(3.39,2.18,1.07,4.34)
(2.80,2.50,0.50,25.0)	(2.64,2.67,0.53,20.7)	(5.87,6.77,5.92,17.34)
(3.00,1.70,0.90,30.0)	(3.22,1.78,0.85,28.2)	(7.48,4.97,5.27,6.15)
(2.50,1.30,2.00,13.0)	(2.53,1.32,2.04,14.0)	(1.20,1.82,2.03,7.48)
(1.00,2.00,2.40,-15.0)	(1.02,2.01,2.39,-14.9)	(1.76,0.67,0.22,0.55)
(2.80,1.70,1.10,35.0)	(2.81,1.74,1.16,36.6)	(0.35,2.46,5.00,4.57)

ellipsoids are varied as $0.5\lambda, 1\lambda, 1.5\lambda, 2\lambda, 2.5\lambda$ and 3λ, and θ is varied as $-40°, -30°, -20°, -10°, 0°, 10°, 20°, 30°$ and $40°$, respectively. All of these a, b, c and θ namely, 1944 different combinations are used as the training data. The conductivity and relative permittivity of the ellipsoid target are set to $1.0\times10^7\mathrm{S/m}$ and $\epsilon = 1.0$, respectively. The observation data are generated by the FDTD method assuming a noiseless situation. The neural network contains three hidden layers, with 30 neurons in the first layer, 20 in the second layer, and 10 in the final layer. Here, $K\Delta R = 1.44\lambda$, and the sample interval of range as $\Delta R = 0.03\lambda$ are set in Eq. (6). Table I lists the parameters of the ellipsoid targets estimated by the trained neural network. The untrained parameters are depicted in red font. From Table I, it can be observed that the time-series based neural network accurately estimated the ellipsoidal parameters. The average relative errors in a, b, c and θ are 2.7%, 2.3%, 1.3% and 6.9%, respectively.

B. Expansion Performance

This subsection presents the expansion results of our proposed method. The transmitting and receiving antenna set is scanned over the area $-2.5\lambda \le x, y \le 2.5\lambda$ at 0.5λ intervals in the x and y directions. Again, the observation data are generated by the FDTD method. Here, the operational frequency band (10dB criteria mostly used in UWB signal) in this simulation is about 2.0 GHZ, and its range resolution is 150 mm. The center frequency is 3 GHz, (corresponding wavelength in the air is 100mm), denoting that its fractional bandwidth is around 66 %.

In RPM imaging, the set of range points $\boldsymbol{q}_{x,x}$ extracted by $s_{x,x}(X, Y, R')$ is used only in the initial 3-D imaging. Figure 13 shows the target points obtained by RPM for the ellipsoid target, where the solid lines show the discrete expression of the true ellipsoidal boundary. Here, $a = 2.5\lambda$, $b = 1.5\lambda$, $c = 1.0\lambda$, $\theta = 0°$, and the y-axis is rotated through $20°$. According to Fig. 13, the target points obtained by RPM cannot sufficiently express target image to recognize the original ellipsoidal shape, while highly reconstruction accuracy is provided. This is because the target is located from sensor location with significant distance around 6λ, and this leads to smaller aperture angle. On the contrary, Fig. 14 shows the image expansion result obtained by the proposed method. Here, the elevation angle of each ellipsoid is limited to $(\phi_E = -7\pi/18)$. Also, the parameter $\sigma_\zeta = 0.25\lambda$and $\gamma = 0.3$ in Eq. (15) are set. Figure 14 indicates that the proposed method correctly expands the target points obtained from the RPM imaging points. Figures 15 and 16 show the target points obtained by RPM and the expansion expression of the proposed method, respectively. The target is the torus shown in Fig. 1. According to these figures, the proposed method significantly enhances the imaging region of the torus boundary, which is dissimilar to an ellipsoid. The expansion errors in Fig. 16 result from the inaccurate estimation of the ellipsoid parameters from time-series data, because each antenna receives multiple reflection echoes within range resolution from the torus boundary, and then, the expansion accuracy depends on the operational bandwidth, naturally. It should be considered that an another cause is the convex boundary based fitting with ellipsoid, namely, the positive principal curvature, while the part of torus boundary has a negative principal curvature, such as saddle boundary. However, a largely deviated artifact of the part of expansion image is efficiently suppressed by introducing the post-processing denoted in Step 7) in the proposed method. It should be also noted that there is accuracy degradation caused by the discrepancy between the reference signal and actual received signal in ranging process with Wiener filtering. However, such kind of ranging inaccuracy is the order of 0.1λ, and affects both RPM and the proposed methods [21], [22]. To prevent this interference effect, the windowing time span for extracting the time series data should be also appropriately determined. The average calculation times for the original RPM and the proposed method after NN learning, are 0.2 sec and 30 sec, respectively, using Intel Xeon CPU E5-1620 v2 3.70 GHz processor, and such calculation time is hardly achieved by the conventional beamforming or Kirchhoff migration algorithms in obtaining the 3-D full image.

We now discuss a noisy situation. Each received signal is subjected to Gaussian white noises $s_{x,x}$, $s_{x,y}$ and $s_{y,y}$. The signal-to-noise ratio S/N is defined as the ratio of the peak instantaneous signal power in all polarization data to the average noise power after applying a matched filter. Figure 18 shows the RPM-obtained target points of a single ellipsoid in the noisy case. The average S/N of $s_{x,y}$ is approximately 20 dB and those of $s_{x,x}$ and $s_{y,y}$ are approximately 50 dB. It should be noted that the above definition is the most strict estimation for S/N, because the matched filter is most noise-robust filter, namely this definition considers the locality of signal in both time and frequency domain. Figure 17 shows an example of received signals assuming S/N=20dB, and it denotes that while signal can be recognized after applying matched filter (denoted as (c)), the raw received signal (b) (before applying matched filter) is more noisy. Such S/N level signal is usually obtained in the real experiment assuming short range sensing (distance from sensor is within 5m), as demonstrated in [10].

Figure 18 indicates that the RPM retains sufficient accuracy even in a noisy situation, while the estimated points expresses only a portion of the whole target shape. Figure 19 shows the expansion results of the proposed method. Although the expansion accuracy is slightly worse than that in the noise-

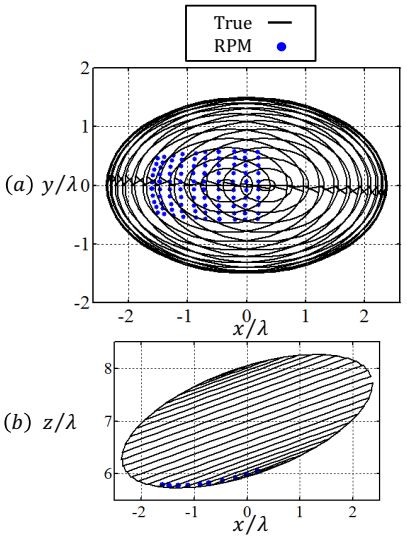

Fig. 13. Target boundary points estimated by RPM method for single ellipsoid target in noiseless situation (a: projection to x-y plane, b: cross-section for y=0 plane.). Solid lines show the discrete expression of true boundary.

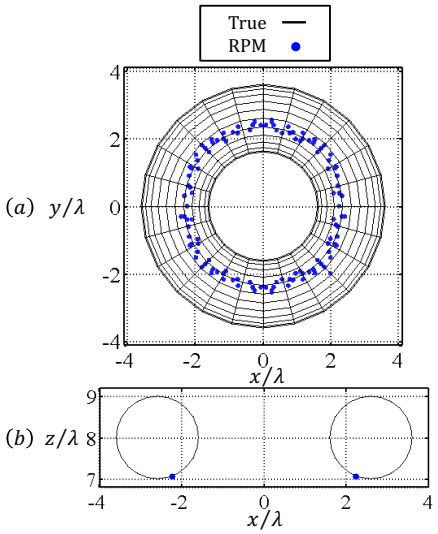

Fig. 15. Target boundary points estimated by RPM method for torus target in noiseless situation (a: projection to x-y plane, b: cross-section for y=0 plane.). Solid lines show the discrete expression of true boundary.

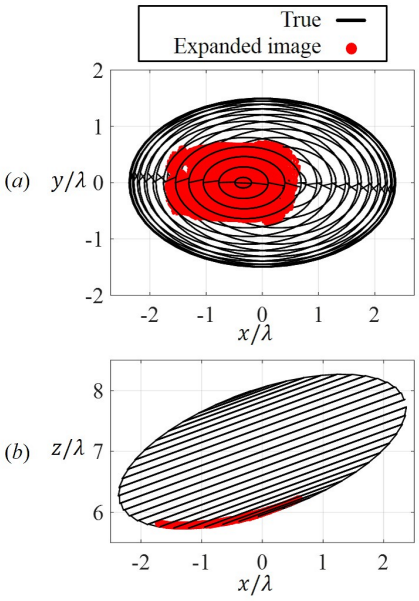

Fig. 14. Expansion result of the proposed method for single ellipsoid target in noiseless situation (a: projection to x-y plane, b: cross-section for y=0 plane.). Solid lines show the discrete expression of true boundary.

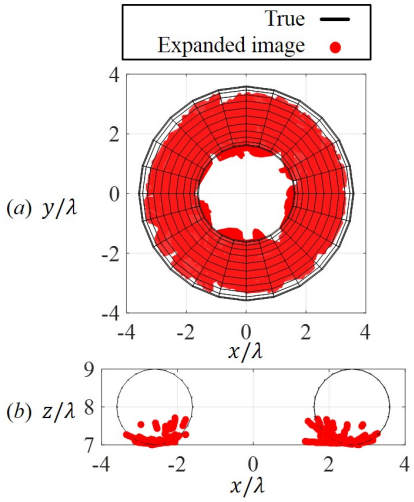

Fig. 16. Expansion result of the proposed method for torus target in noiseless situation (a: projection to x-y plane, b: cross-section for y=0 plane.). Solid lines show the discrete expression of true boundary.

less situation, the proposed method significantly expanded the region that can be imaged, while maintaining acceptable accuracy. Figs. 20 and 21 show the results of imaging a torus by RPM and by the proposed expansion method, respectively. The approximate average S/N of $s_{x,y}$, $s_{x,x}$ and $s_{y,y}$ are 20 dB, 32 dB, and 32 dB, respectively. Comparing these results to the noiseless case, the noise did not severely degrade the image expansion, and the expansion of the image is retained.

Finally, the image expansion is quantitatively analyzed by investigating the effective reconstruction image region, namely, the expansion effect. For this evaluation, first, a whole true target boundary denoted as $\Omega_{\rm all}^{\rm true}$ is divided into small regions with the same area as $\Delta\Omega_i^{\rm true}, (i = 1, 2, \cdots, N_{\rm tar})$. A whole target boundary region is expressed as

$$\Omega_{\rm all}^{\rm true} = \bigcup_i \Delta\Omega_i^{\rm true}. \tag{17}$$

Also, the center point for the region $\Omega_i^{\rm true}$ is defined as $\boldsymbol{p}_i^{\rm true}$. Then, for the k-th estimated target point denoted as $\boldsymbol{p}_k^{\rm est}$, the

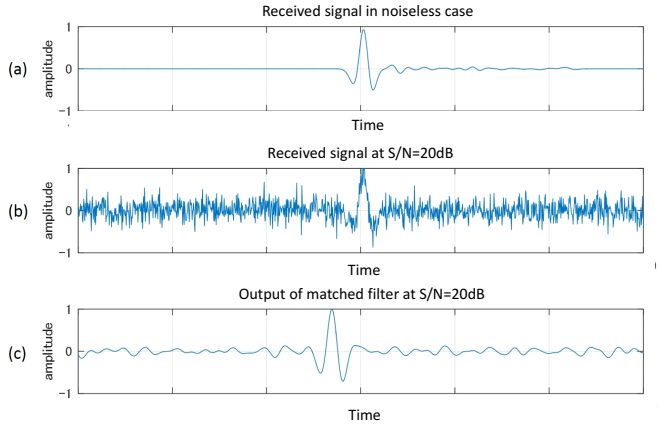

Fig. 17. Example of received signal. (a): Received signal in noiseless case. (b): Received signal in S/N=20dB. (c): Output of matched filter for received signal illustrated in (b).

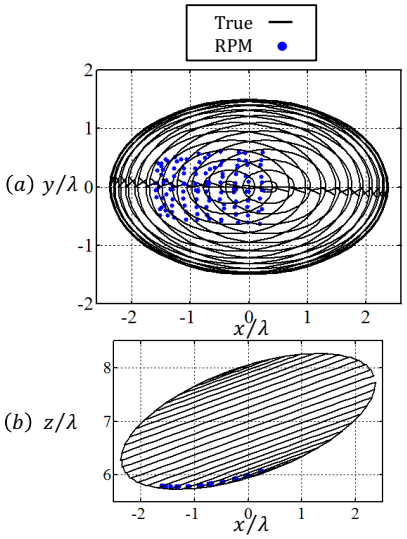

Fig. 18. Target boundary points estimated by RPM method for ellipsoid target in S/N=20dB (a: projection to x-y plane, b: cross-section for y=0 plane.). Solid lines show the discrete expression of true boundary.

estimated effective image area $\hat{\Omega}_k^{\text{eff}}$ is defined as;

$$\hat{\Omega}_k^{\text{eff}} = \left\{ \bigcup_i \Delta\Omega_i^{\text{true}} \;\middle|\; \|\boldsymbol{p}_i^{\text{true}} - \boldsymbol{p}_k^{\text{est}}\| \le \delta_p \right\}, \tag{18}$$

where δ_p is threshold for extracting effective image region, which is empirically determined as $\delta_p = 0.2\lambda$, in this case. The effective image area $\hat{\Omega}^{\text{eff}}$ composed of all target points is defined as;

$$\hat{\Omega}^{\text{eff}} = \bigcup_k \hat{\Omega}_k^{\text{eff}}. \tag{19}$$

As the evaluation value for image expansion effect, the image

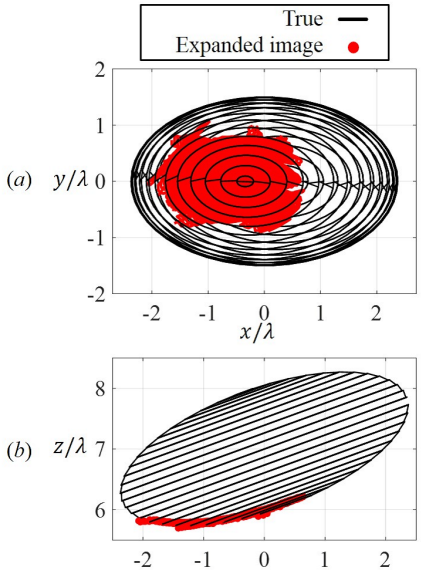

Fig. 19. Expansion result of the proposed method for ellipsoid target in S/N=20dB (a: projection to x-y plane, b: cross-section for y=0 plane.). Solid lines show the discrete expression of true boundary.

TABLE II
VALUE OF $P_a[\%]$ OF EACH METHOD.

S/N	∞		20dB($s_{x,y}$)	
Target	Ellipsoid	Torus	Ellipsoid	Torus
RPM	15.9 %	7.2 %	16.3 %	7.6 %
Proposed	21.6 %	34.9 %	26.7 %	35.4 %

expansion ratio is defined as;

$$P_{\text{a}} = \frac{S_{\text{eff}}}{S_{\text{true}}}, \tag{20}$$

where S_{true} and S_{eff} denote the areas of $\Omega_{\text{all}}^{\text{true}}$ and $\hat{\Omega}^{\text{eff}}$, respectively. Figure 22 illustrates for the effective image area $\hat{\Omega}_k^{\text{eff}}$ for each target point $\boldsymbol{p}_k^{\text{est}}$. The percentage image expansion ratio P_{a} in the absence and presence of noise is computed for each method, and the results are summarized in Table II. Clearly, the proposed method significantly expands the target image, even when the target deviated from an ellipsoid.

However (see also Figs. 16 and 21), in the case of torus shaped target, there are non-negligible errors in expansion. Although it significantly enhances the image expansion ratio, expansion accuracy requires an additional evaluation criterion. The error in the image reconstruction is given by

$$\text{e}(\boldsymbol{p}_k^{\text{est}}) \equiv \min_{\boldsymbol{p}_{\text{true}}} \left\|\boldsymbol{p}_k^{\text{est}} - \boldsymbol{p}^{\text{true}}\right\| \quad (k = 1, 2, \ldots, N_{\text{est}}), \tag{21}$$

where $\boldsymbol{p}^{\text{true}}$ denotes the true target points in discrete expression with sufficiently dense sample and N_{est} denotes the total number of the estimated points. Figures 23 and 24 plot the number of estimated points with error $\text{e}(\boldsymbol{p}_k^{\text{est}})$ in expansions of ellipsoidal and toroidal targets, respectively. While the proposed method and RPM yield the same reconstruction accuracy of ellipsoidal targets, RPM better reconstructs the toroidal target, because of the aforementioned interference

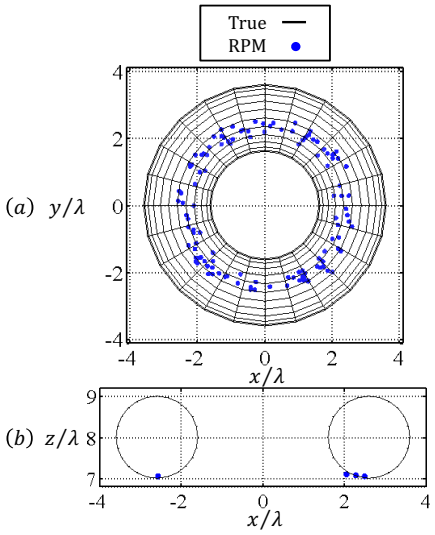

Fig. 20. Target boundary points estimated by RPM method for torus target in S/N=20dB (a: projection to x-y plane, b: cross-section for y=0 plane.). Solid lines show the discrete expression of true boundary.

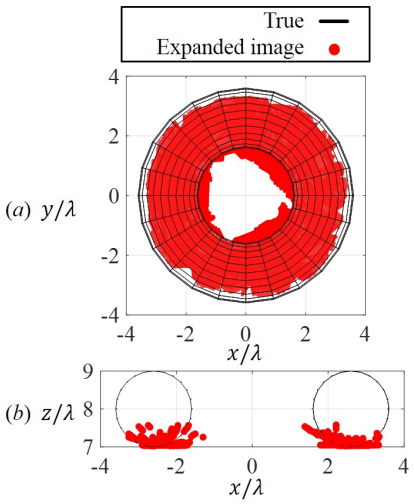

Fig. 21. Expansion result of the proposed method for torus target in S/N=20dB (a: projection to x-y plane, b: cross-section for y=0 plane.). Solid lines show the discrete expression of true boundary.

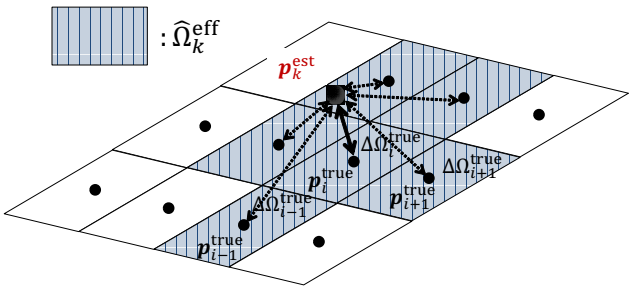

Fig. 22. Spatial relationship of effective image area $\hat{\Omega}_k^{\mathrm{eff}}$ for each target point $\boldsymbol{p}_k^{\mathrm{est}}$.

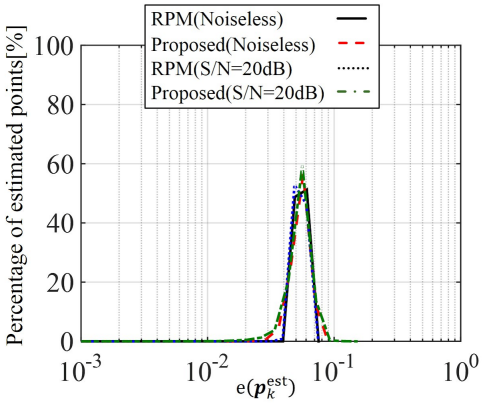

Fig. 23. Number of the estimated target points of ellipse target in noiseless and noisy situation.

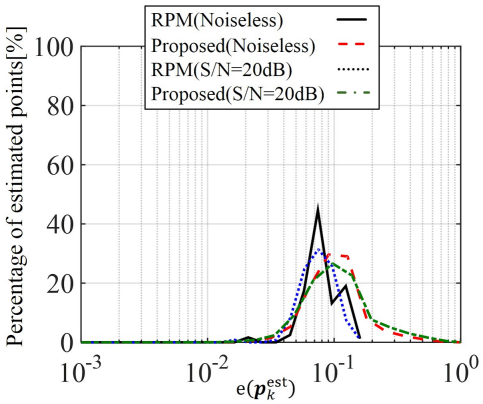

Fig. 24. Number of the estimated target points of torus target in noiseless and noisy situation.

effect in the proposed method. However, the maximum error in the toroidal target is within 1 λ, and the apparent expanded image does not markedly deviate from the actual target shape. Table III lists the percentage of estimated target points satisfying $\mathrm{e}(\boldsymbol{p}_k^{\mathrm{est}}) \leq 0.2\lambda$ in the ellipsoidal and toroidal cases. Combining this evaluation and the image expansion ratio denoted as P_a shown in Table II, the proposed method achieves an effective target image expansion without sacrificing a serious accuracy degradation. Clearly, the percentage of accurately estimated target points (expanded points) is reduced when our method is applied to toroidal objects. This inaccuracy must be addressed in our future work.

C. Evaluation for edge preserving property

To demonstrate the edge preserving property of the proposed method, this section introduces the example for cylinder shape target. Figures 25 and 26 show the RPM-obtained target points and the expanded image by the proposed method, respectively. A noiseless situation is assumed. As shown in Fig. 25, the RPM holds a high accuracy even around the end of cylinder target, but expresses a part of cylinder shape. Figure 26 shows that our proposed method expands the cylinder shape without over expansion the edge region, where the expansion area is limited along a larger curvature direction in Eq. (13). The ratio

TABLE III
RATE OF ESTIMATED TARGET POINTS THAT SATISFY E $\leq 0.2\lambda$.

S/N	∞		20dB($s_{x,y}$)	
Target	Ellipsoid	Torus	Ellipsoid	Torus
RPM	100 %	100 %	100.0 %	100 %
Proposed	100 %	94.3 %	100 %	90.6 %

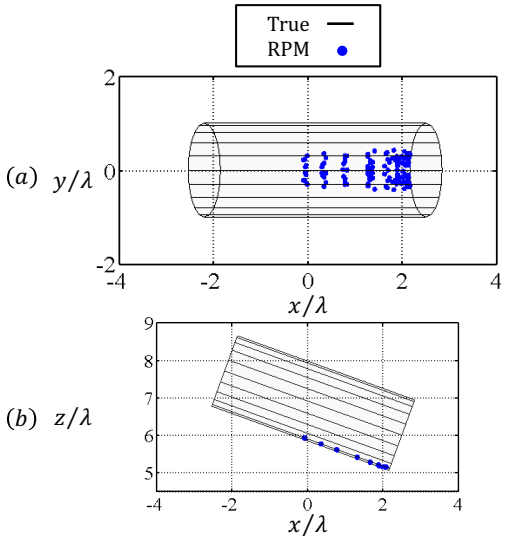

Fig. 25. Target boundary points estimated by RPM method for cylinder target. Solid lines show the discrete expression of true boundary.

that the reconstructed points satisfies that the errors less than 0.2λ, are 100 % for both the conventional and the proposed methods. The image expansion ratios denoted as P_a are 6.9 % for the original RPM and 14.4 % for the the proposed method, respectively. These quantitative evaluations also show that our method successfully expands the cylinder shape target, which guarantees an edge preserving property.

VI. CONCLUSION

This paper proposed a novel 3-D image expansion method that incorporates the RPM method but exploits the fully polarimetric dataset. In a time-series data analysis of fully polarimetric data, the co-polarization and cross-polarization data were strongly correlated with the radius and rotation angle of a single ellipsoid. By neural-network learning of the ellipsoid parameters, the target was accurately estimated from the time-series data only received by a single antenna. Next, to expand the reproduced image, we combined the RPM method with single ellipsoid estimation by the fully polarimetric data. By using multiple partial ellipsoidal surfaces to the RPM target points, we exploited the one-to-one correspondence between the target and the range points, which makes us possible to connect the polarimetric data to each target point. In addition, to deal with a target having edge or ridge, our method adaptively change the expansion area with the curvature analysis provided by the RPM feature. Finally, in FDTD simulations,

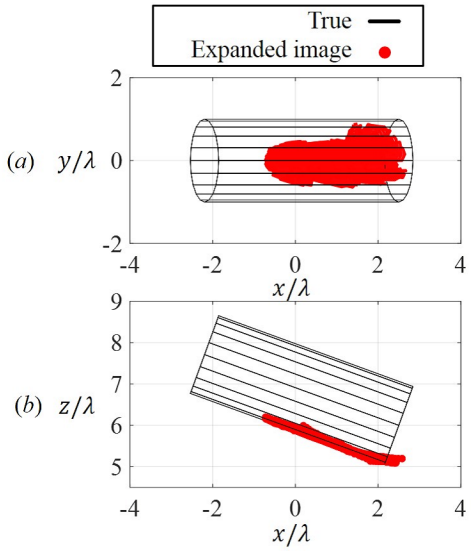

Fig. 26. Expansion result of the proposed method for cylinder target (a: projection to x-y plane, b: cross-section for y=0 plane.).

we verified that the image expansion ratio is much higher in the proposed method than in the original RPM method, even for decidedly non-ellipsoidal target shapes, without serious accuracy degradation. The extrapolation level of the proposed method depends on the parameter ϕ_{E} in Eq. (12), which determines the extrapolation area of the partial ellipsoid. If we set the ϕ_{E} larger, there is risk for generating false image deviated from the actual boundary. Then, the adjustment of the parameter ϕ_{E} is required to keep balance between the accuracy and expansion effect. As a result, the expansion effect in the case of ellipsoid target seems to be an interpolated image, this is because the reflection strength from a ellipsoid is comparatively smaller than that of torus or cylinder object, where the signal strength is one factor to determine the size of each fitted ellipsoid.

Note that, the proposed method does not need to decompose co-pol and cross-pol components from the measured data, which are generally difficult in non-planar incident wave case. This is because this method requires a relative quantity between the reference (training) signal and the received signal, in terms of the x and y components of electric fields. However, the accuracy for polarimetric measurement would affect the final image in both RPM and the proposed method. It is also noted that the training data in neural network is only limited to ellipsoid, then, to deal with the general boundary shape having a concave or saddle boundary, the training data from object with such negative principal curvatures should be processed. It is our important future work. Further investigation for such effect should be done in our future work through real experiments.

ACKNOWLEDGMENT

This work is supported in part by the Grant-in-Aid for Scientific Research (B) (Grant No. 22360161), the Grant-in-Aid for Young Scientists (B) (Grant No. 23760364), promoted by Japan Society for the Promotion of Science (JSPS), the

Research Grant promoted by KDDI funcation, Support Center for Advanced Telecommunications Technology Research Foundation (SCAT) and the Murata Science Foundation.

REFERENCES

[1] D. L. Mensa, G. Heidbreder and G. Wade, "Aperture Synthesis by Object Rotation in Coherent Imaging," *IEEE Trans.NuclearScience Sensing*., vol.27, no.2, pp.989-998, Apr. 1980.

[2] A. J. Devaney, "Time Reversal Imaging of Obscured Targets From Multistatic Data", *IEEE Trans.Antennas Propag*., vol.53, no.5, pp.1660-1610, May, 2005.

[3] E. A. Marengo, F. K. Gruber, and F. Simonetti, "Time-Reversal MUSIC Imaging of Extended Targets", *IEEE Trans.Image Process*., vol.16, no.8, pp.1967-1984, Aug, 2007.

[4] J. M. Lopez-Sanchez, J. Fortuny-Guasch, "3-D radar imaging using range migration techniques," *IEEE Trans. Antennas Propag.*, Vol. 48, No. 5, pp. 728?737, May 2000

[5] J. Song, Q. H. Liu, P. Torrione, and L. Collins, "Twodimensional and three dimensional NUFFT migration method for landmine detection using ground-penetrating radar", *IEEE Trans.Geosci. RemoteSens*., vol.44, no.6, pp.1462-1469, Jun, 2006.

[6] F. Soldovieri, A. Brancaccio, G. Prisco, G. Leone, and R. Pieri, "A Kirchhoff-based shape reconstruction algorithm for the multimonostatic configuration: The realistic case of buried pipes", *IEEE Trans.Geosci. RemoteSens*., vol.46, no.10, pp.3031-3038, Oct, 2008.

[7] T. Sakamoto, "A fast algorithm for 3-dimensional imaging with UWB pulse radar systems," *IEICE Transactions on Communications*, vol. E90-B, no. 3, pp. 636?644, March 2007

[8] S. Kidera, T. Sakamoto, and T. Sato, "Accurate UWB Radar 3-D Imaging Algorithm for Complex Boundary without Range Points Connections," *IEEE Trans. Geosci. & Remote Sens.*, vol.48, no. 4, pp. 1993–2004, Apr., 2010.

[9] S. Kidera, T. Kirimoto, "Efficient 3-dimensional Imaging Method Based on Enhanced Range Points Migration for UWB Radars," *IEEE Geosci. & Remote Sens. Letters*, vol.10, no. 5, pp. 1104–1108, Sep., 2013.

[10] S. Kidera, T. Sakamoto and T. Sato, "Super-Resolution UWB Radar Imaging Algorithm Based on Extended Capon with Reference Signal Optimization," *IEEE Trans. Antennas. & Propagation.*, vol.59, no. 5, pp. 1606–1615, May, 2011.

[11] R. Salman, I. Willms, "3D UWB Radar Super-Resolution Imaging for complex Objects with discontinous Wavefronts," 2011 IEEE International Conference on Ultra-Wideband (ICUWB), Sep. 2011.

[12] S. S. Fayazi, J. Yang, H-S. Lui, "UWB SAR Imaging of Near-Field Object for Industrial Process Applications," 2013 7th European Conference on Antennas and Propagation (EuCAP) Apr. 2013.

[13] H. Taki, S. Tanimura, T. Sakamoto, T. Shiina and T. Sato, "Accurate ultrasound imaging based on range point migration method for the depiction of fetal surface," Journal of Medical Ultrasonics, September 2014.

[14] Y. Abe, S. Kidera and T. Kirimoto, "Accurate Image Expansion Method Using Range Points Based Ellipse Fitting for UWB Imaging Radar," *IEICE Trans. & Commun.*, vol. E95-B, no. 7, pp. 2424-2432, July., 2012.

[15] D. Damyanov, T. Schultze, I. Willms and R. Salman, "Super-Resolution Feature Extraction Imaging Algorithm for complex Objects" *IEEE Proc. of 2014 IEEE International Conference on Ultra-WideBand (ICUWB)* , Sep. 2014.

[16] R. Salman, I. Willms, T. Sakamoto, T. Sato, and A. Yarovoy, "3D imaging of a manmade target with weak scattering centres by means of UWB-radar," *IEEE Proc. of 2013 IEEE International Conference on Ultra-WideBand (ICUWB)* , Sep. 2013.

[17] J. Kruk, C. P. A. Wapenaar, J. T. Fokkema and P. M. Van den Berg, "Three-dimensional imaging of multicomponent ground-penetrating radar data", *Geophysics* 68 (4), 1241-1254, 2003.

[18] A. Yarovoy, A. Schukin, I. Kaploun and L. Ligthart, "High-resolution full-polarimetric video impulse radar for landmine detection", *2002 International Radar Conference*, pp. 205 – 209, 2002;

[19] V. Kovalenko, A. Yarovoy and L. Ligthart, "Polarimetric feature fusion in GPR for landmine detection, " *IEEE International Geoscience and Remote Sensing Symposium, IGARSS 2007*, pp. 30-33, 2007;

[20] R. Salman and I. Willms, "Exploitation of polarimetry in short range 3D UWB-radar object imaging", *2012 International Conference on 3D Imaging (IC3D)*, 2012.

[21] S. Kidera, T. Sakamoto and T. Sato, "High-resolution and Real-Time 3-D Imaging Algorithm with Envelope of Spheres for UWB Radars", *IEEE Trans. Geoscience and Remote Sensing*, vol.46, no.11, pp.3503–3513, Nov, 2008.

[22] S. Kidera, T. Sakamoto and T. Sato, "A high-resolution imaging algorithm without derivatives based on waveform estimation for UWB pulse radars", *IEICE Trans. Commun.*, vol. E89-B, no. 9, pp. 2588-2595, Sep, 2006.

[23] S. Kidera, T. Sakamoto, and T. Sato, " A robust and fast imaging algorithm with an envelope of circles for UWB pulse radars, " IEICE Trans. Commun., vol. E90-B, no. 7, pp. 1801–1809, Jul. 2007.

PLACE PHOTO HERE

Ayumi Yamaryo received her B.E. and M.E. degrees in Electronic Engineering from University of Electro-Communications in 2013 and 2015, respectively. She joined Mitsubishi Electric Corp. in 2015.

PLACE PHOTO HERE

Tatsuo Takatori received his B.E. degrees in Communication Engineering and Informatics from University of Electro-Communications in 2016. He is currently studying for an M.E degree at Graduate School of Informatics and Engineering, University of Electro-Communications. His current research interest is advanced radar signal processing for UWB radar systems.

PLACE PHOTO HERE

Shouhei Kidera received his B.E. degree in Electrical and Electronic Engineering from Kyoto University in 2003 and M.I. and Ph.D. degrees in Informatics from Kyoto University, Kyoto, Japan, in 2005 and 2007, respectively. He has been with Graduate School of Informatics and Engineering, the University of Electro-Communications, Tokyo, Japan, since 2009, and is currently an Associate Professor. He has been stayed at the Cross-Disciplinary Electromagnetics Laboratory in the University of Wisconsin Madison as the visiting researcher in 2016. His current research interest is in advanced radar signal processing or electromagnetic inverse scattering issue for ultra wideband (UWB) three-dimensional sensor or bio-medical applications. He was a recipient of the 2012 Ando Incentive Prize for the Study of Electronics, 2013 Young Scientist's Prize by the Japanese Minister of Education, Culture, Sports, Science and Technology (MEXT), and 2014 Funai Achievement Award. He is a member of the Institute of Electronics, Information, and Communication Engineers of Japan (IEICE), and the Institute of Electrical Engineering of Japan (IEEJ).

PLACE
PHOTO
HERE

Tetsuo Kirimoto received the B.S. and M.S. and Ph.D degrees in Communication Engineering from Osaka University in 1976, 1978 and 1995, respectively. During 1978-2003 he stayed in Mitsubishi Electric Corp. to study radar signal processing. From 1982 to 1983, he stayed as a visiting scientist at the Remote Sensing Laboratory of the University of Kansas. From 2003 to 2007, he joined the University of Kitakyushu as a Professor. Since 2007, he has been with the University of Electro-Communications, where he is a Professor at the Graduate School of Informatics and Engineering. His current study interests include digital signal processing and its application to various sensor systems. Prof. Kirimoto is a member of the Institute of Electronics, Information, and Communication Engineers of Japan (IEICE), and a member of SICE (The Society of Instrument and Control Engineers) of Japan.